A comprehensive investigation on microstructure and mechanical properties optimisation of 316L stainless steel produced by laser-based powder bed fusion

Ehsan Farabi
Institute for Frontier Materials, Deakin University, Melbourne, Australia, and School of Materials Science and Engineering, UNSW Sydney, Sydney, Australia

Mahyar Khorasani
Centre for Additive Manufacturing, School of Engineering, Royal Melbourne Institute of Technology, Melbourne, Australia

Ahmad Mirzai
Department of Materials Science and Engineering, University of California Irvine, Irvine, California, USA

Amir Hossein Ghasemi
Australian Institute of Science and Technology, Melbourne, Australia

Guy Littlefair
School of Engineering, The University of Western Australia, Perth, Australia

Eric MacDonald
Faculty of Engineering, The University of Texas at El Paso, El Paso, Texas, USA

Martin Leary
Centre for Additive Manufacturing, School of Engineering, Royal Melbourne Institute of Technology, Melbourne, Australia

Ian Gibson
Department of Fraunhofer Innovation Platform for Advanced Manufacturing, University of Twente, Enschede, The Netherlands

Stuart Bateman
Centre for Additive Manufacturing, School of Engineering, Royal Melbourne Institute of Technology, Melbourne, Australia, and

Bernard Rolfe
School of Engineering, Deakin University, Melbourne, Australia

Abstract

Purpose – This study aims to introduce an algorithm that can successfully define optimum laser-based powder bed fusion (LB-PBF) processing and post-heat treatment parameters for manufacturing 316L stainless steels with limited energy usage and enhanced properties.

Design/methodology/approach – Taguchi's design of the experiment (DoE) was elaborated to define the ideal LB-PBF process and heat treatment parameters. Based on the DoE and experimental results, the LB-PBF energy density between 6.7 J/mm^3 and 14.7 J/mm^3 produced parts with a volumetric mass density of 98.8% or higher. The authors' proposed processing window shows 316 L manufactured products can reach the highest mechanical strength reported in literature.

Findings – The microstructure characteristics of the enhanced 316L builds showed characteristic dislocation density, grain size and texture features. The proposed heat treatments at 650, 870 and 1,150 °C results in preferential grain growth up to approximately 45 μm, reorienting the as-built grain structure from <100> to <101> components. This promoted mechanical twinning propensity and the dynamic Hall–Petch effect, resulting in significant improvements in the mechanical properties.

The current issue and full text archive of this journal is available on Emerald Insight at: **https://www.emerald.com/insight/1355-2546.htm**

Rapid Prototyping Journal
32/11 (2026) 146–162
Emerald Publishing Limited [ISSN 1355-2546]
[DOI 10.1108/RPJ-12-2024-0519]

Received 17 December 2024
Revised 30 December 2025
14 April 2026
Accepted 14 May 2026

Originality/value – The manufactured parts in the optimised conditions achieved improvement in ultimate tensile strength (970 MPa) and elongation (32%), representing a noticeable strength–ductility combination for LB-PBF of 316L.

Keywords Additive manufacturing, Heat treatment, Laser-based powder bed fusion, Microstructure, Tensile properties, Residual stress

Paper type Research paper

1. Introduction

The 316L stainless steel (316L SS) is one of the most commonly used materials in engineering applications and has been successfully produced using a variety of additive manufacturing techniques. The laser-based powder bed fusion (LB-PBF) method has become highly regarded for manufacturing 316L SS due to its ability to create a unique hierarchical microstructure. This microstructure contributes to exceptional corrosion resistance and mechanical properties in the final printed product (Gibson *et al.*, 2021). This largely includes large columnar grains (100 s microns via epitaxial growth during solidification) and a sub-structure consisting of approximately 1 μm diameter cellular network of high dislocation densities with Mo and Cr segregation (Bajaj *et al.*, 2020; Wang *et al.*, 2018). The industrial breakthrough of LB-PBF parts is still limited by the challenges of producing structures with minimal defects and heterogeneous structures, achieving mechanical properties comparable to conventional processes and relying on labour-intensive post-process procedures like powder removal, heat treatment and machining (Schneck *et al.*, 2021; SN, 2024). The key to overcoming these issues lies in selecting the best LB-PBF method and post-process settings. Hence, the complex interaction among the microstructure constituents and LB-PBF processing parameters (i.e. process-microstructure-property relationships) needs to be clearly understood to optimise the process for printing defect-free 316L products with enhanced properties (Liverani *et al.*, 2017; Kok *et al.*, 2018).

The ability to control the LB-PBF process parameters (laser power, hatch distance, scan speed) and scanning strategies (the path of the laser vector) at specific layers, provides control over the complex thermal history and, consequently, the microstructure development. From one point, defects such as lack of fusion, keyhole and balling phenomenon may occur due to poorly chosen combination of parameters (Heeling and Wegener, 2018; Ronneberg *et al.*, 2020; Röttger *et al.*, 2016). The high thermal gradients produced by the localised and successive laser melting process can also generate thermal residual stresses as high as 500 MPa and lead to delamination, distortion and deterioration in the printed 316L SS product (Tapia and Elwany, 2014; DebRoy *et al.*, 2018; Chen *et al.*, 2018). On the other hand, the process parameters, such as laser power and scanning speed, play a crucial role in achieving and maintaining an acceptable density for the manufactured 316L SS parts. Parameters such as volumetric energy density are generally introduced to correlate processing parameters to the microstructure and properties of LB-PBF 316SS (Read *et al.*, 2015). Earlier research has shown that maintaining the energy density within the range of 100–110 J/mm^2 can result in defect-free 316L SS parts (Cherry *et al.*, 2015; Wang *et al.*, 2016; Sander *et al.*, 2017); while deviating to excessively higher or lower energy densities may increase the likelihood of porosity formation (Leicht *et al.*, 2020).

Apart from processing defects, the performance of the printed part is also influenced by its microstructural characteristics. The heat flow, competitive growth mechanisms and epitaxial grain growth result in the formation of elongated grains with a preferential crystal orientation along the building direction (Sun *et al.*, 2018; Bahl *et al.*, 2019). These coarse grain structures are largely aligned with a specific crystallographic orientation, which can have diverse impacts on the mechanical performance of the material. The commonly observed <100> textures in additive manufacturing (AM) of 316L SS are generally associated with lower strength and ductility (Suryawanshi *et al.*, 2017; Niendorf *et al.*, 2013). However, altering the processing parameters to induce the <110> components has been demonstrated to enhance the propensity for mechanical twinning, which in turn results in twinning-induced plasticity and improved mechanical properties (Marattukalam *et al.*, 2020). Moyle *et al.* (2022) revealed that increasing scan speed at low laser powers (i.e.<200 W) realigns the austenitic grains of 316L SS along the <110> orientations, while at higher laser powers, grains generally lie between the <100> and <101> orientations. On the other hand, the unidirectional scanning strategy for face-centered cubic (FCC) materials (i.e. austenitic steels and model Ni alloys) has been associated with epitaxial grain growth and a strong fibre texture, while the bidirectional strategies can lead to mixed <100> and <110> textured grains (Marattukalam *et al.*, 2020; Thijs *et al.*, 2013; Dinda *et al.*, 2012; Wei *et al.*, 2015). Scanning rotation also affects the melt pool geometry and the grain growth pattern during the LB-PBF process. Previous studies have observed that single- or multiple 180° scanning rotations can result in strong <100> or <110> components (Sun *et al.*, 2018; Leicht *et al.*, 2020; Andreau *et al.*, 2019). Marattukalam *et al.* (2020), on the other hand, showed that adding 67° rotations can effectively break up columnar grains, resulting in the creation of finer structures and improving the fibre texture in the printed 316L material. Across the whole spectrum of potential rotations and process parameters, little is known about how the interplay between the rotation angle, laser power, hatch distance and scan speed might impact the prevailing microstructure and optimise the properties of the 316L printed product.

In addition, post-process heat treatment can alleviate the defect structures, residual stresses, elemental segregation, microstructure heterogeneities and texture anisotropy (Tapia and Elwany, 2014; DebRoy *et al.*, 2018; Chen *et al.*, 2018). Heat treatment up to 1,400°C temperatures annihilates segregation and cellular network of the as-printed 316L SS and results in complete recrystallisation and grain growth (Lou *et al.*, 2018; Laleh *et al.*, 2019; Yadollahi *et al.*, 2015; Chao *et al.*, 2021). However, the as-printed microstructure exhibits stability when subjected to annealing at temperatures of up to

700°C (Ronneberg et al., 2020; Salman et al., 2019). These treatments enhance ductility while ensuring that strength is retained without substantial compromise. Despite these advancements, the effect of heat treatment on the highly contrasting microstructures developed via various LB-PBF processing parameters is still uncertain. This points out the requirement to assess many facets of this complex manufacturing technique and establish a coherent correlation between the process, post-process, microstructure and performance of 316L products.

Accordingly, the various aspects that affect the printing of a high-quality 316L SS product have rendered universal and optimum manufacturing conditions difficult to obtain. Previous studies have mainly focused on the effect of one or two aspects of material synthesis (i.e. process parameters, scanning strategy or post-processing) on the resultant microstructure and mechanical or corrosion properties. However, these aspects all influence microstructure and properties, with likely interrelated effects. This research is the extension of our previous study, which was focused on characterising melt pools in LB-PBF of stainless steel 316L by developing analytical models for meltpool temperatures (Khorasani et al., 2021) . In this study, we aim to investigate the optimised LB-PBF conditions of 316L SS for enhanced mechanical properties through using extensive microstructure analysis. The experimental array comprises laser power, scan speed, hatch space and laser pattern angle, along with different post-heat treatment processes to establish a processing-property relationship and an in-depth understanding of the evolution of the heat-treated microstructures (e.g. phase composition, grain morphology, grain boundary characteristics and texture analysis). The findings in the current work enable manufacturers to systematically optimise the processing parameters for the superior properties of 316L SS engineering parts.

2. Experimental setup

2.1 Powder material and LB-PBF operation

316L SS samples were printed on a Renishaw AM 400 system in an Argon atmosphere. The laser spot diameter has been set at a constant value of 100 μm for all test cases. The machine was equipped with an ytterbium solid laser that works at a 1,060 nm wavelength with a maximum power of 400 W. The printing chamber is vacuumed to 1% oxygen and then filled with argon to prevent the chemical reaction between the powder elements and the oxygen. The 316L SS powder provided by Renishaw, with an average particle size of 30 μm and the chemical composition of Table 1, was used for the LB-PBF process. The gas-atomised powder was mixed with virgin and recycled powder in a ratio of 70/30%. A 316L SS build plate was preheated to 170°C before the printing process. Preheating reduces the high cooling rate between the first layers and the build plate and decreases shrinkage forces and the chances of distortion. The printed samples' relative density was then determined using the Archimedes method. The samples were subjected to a cleaning process and then submerged in distilled water using an electronic densimeter (Qualitest Model SD-200 L) with a precision of 0.0001 g/cm^3. The measurements are calibrated based on the standard 316 L SS density in mill annealed state (8.00 g/cm^3).

Based on the proposed DoE and American society for testing materials (ASTM) E8 standards for tensile testing, 25 flat tensile samples were printed along the *Y* direction (Astm, 2016). Figure 1(a) shows the printing orientation and dimension of the tensile test samples and scanning pattern. A meander laser scanning path with 67° rotation between the two subsequent layers was used to efficiently break the columnar grain formed during the LB-PBF process [Figure 1(b)] (Marattukalam et al., 2020).

2.2 Design of experiments

Full factorial DoE designs can provide more efficient and reliable experiments. Still, the total test number and the experimentation time increase, making the test difficult to perform. In this experiment, five parameters at five levels, including laser power, scan speed, hatch space, scanning pattern angle and heat treatment, were selected, making a total test number of $5^5 = 3125$. Taguchi DoE can considerably reduce the experiment's time and cost while insignificantly decreasing its accuracy. The current work selects a Taguchi L25 DoE for five inputs and a single output. It should be noted that details about the factor/level selection, L25 array construction, replication strategy and the thermophysical formulation linking process inputs to melt-pool temperature for this statistically driven Taguchi-based workflow have been previously presented in a prior publication by the authors (Khorasani et al., 2021). Here, 75 optimised printing conditions are obtained based on the DoE results (Table 2). It should be noted that two different angular parameters are being used in this study. The meander scanning strategy with a fixed 67° rotation between successive layers is applied to all printing conditions. This inter-layer rotation was not part of the design of experiments and was kept constant throughout the study to minimise texture anisotropy and disrupt continuous columnar grain growth, following previous findings (Marattukalam et al., 2020). On the other hand, the "Scanning Pattern Angle" used in DOE and listed in Table 2 refers to the in-plane orientation of the laser scan vectors within each individual layer, relative to the *x*–*y* build platform. This angle was treated as a variable in the Taguchi DOE to investigate its influence on melt pool

Table 1 Composition (Wt.%) of the 316 = L SS powder

Element	Fe	C	Cr	Ni	Mo	Mn	Si	Cu	Co
Wt.%	Bal.	0.03	17.92	11.59	2.13	1.03	0.77	0.48	<0.35

Figure 1 (a) The schematic illustration of as-built 316L, (b) LB-PBF Scan pattern and (c) wire-cut tensile test sample dimensions

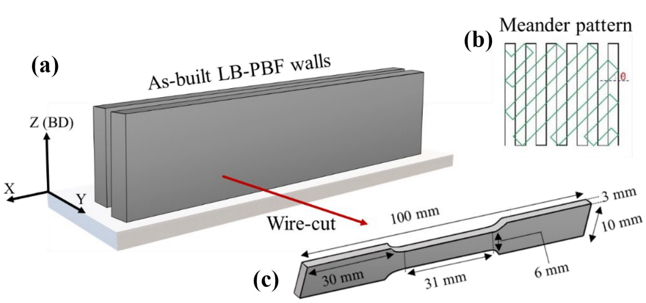

Table 2 The selected process and post-process parameters for Taguchi L25 DOE. (layer thickness was selected as a constant value of 40 μm for all experiments)

Laser power (W)	Scan speed (mm/s)	Hatch spacing (μm)	Scanning pattern angle (°)	Heat treatment temperature (°C)	Average relative density (%)
150	650	60	36	20	98.34
175	700	65	40	425	98.74
200	750	70	45	650	98.78
225	800	75	60	870	98.96
250	850	80	72	1150	98.99

geometry and microstructure. After each layer is completed at its specified scanning angle, the next layer is additionally rotated by 67° regardless of the in-plane angle assigned in Table 2.

2.3 Post-processing (heat treatment)

A fluidised bed furnace consisting of solid particles such as aluminium oxide and Silica was used for heat treatments. The atmosphere of the chamber was controlled by filling it with nitrogen gas. This technique leads to macroscopic separation of the particles and produces uniform treatment on the bulk of the components. The as-built parts were heated up to 425°C, 650°C, 870°C and 1,150°C for two hours, followed by air cooling to room temperature. Heating the parts to 425°C provides stress relief and is extensively used to enhance dimensional stability and reduce stress corrosion cracking in 316L SS. The heat treatments at 650°C and 870°C are associated with the minimum and maximum temperature of sensitising and 1150°C is in the range of solution treatment, which can produce a homogeneous microstructure for the as-built material (Cui *et al.*, 2021; Ebling and Scheil, 1965). Two hours of heat treatment followed by air cooling were selected for 25 samples with three repetitions (a total of 75 samples, Table S1). The two hour dwell across the heat treatment temperatures were used to balance recovery/recrystallisation and homogenisation while avoiding over-sensitisation (Ebling and Scheil, 1965). This aligns with TTS guidance for 316 L and with common LPBF-316L practice, where approximately 2 h holds are reported to enable dislocation recovery and partial recrystallisation within 650–870°C while providing effective solutionising/homogenisation of the AM substructure at 1,150°C (Chao *et al.*, 2021; Laleh *et al.*, 2021).

2.4 Tensile test

To analyse the mechanical performance of the built parts, tensile tests were performed at ambient temperature using a load frame Instron 8801-100KN testing machine equipped with Bluehill software and hydraulic. The gauge length and pre-load were reset before each test to compensate for the tension on the jaws. Tensile samples had a gauge length of approximately 31 mm and the tests were executed at a strain rate of 0.03 s^{-1} [Figure 1(c)]. The detailed dimensions of the tensile samples are depicted in Figure 1(a). Tensile tests were conducted on three independently fabricated specimens per condition after heat treatment to ensure reproducibility and statistical robustness.

2.5 Microstructure analysis

The microstructure of the as-printed and heat-treated samples was examined on different sections of the printed product (i.e. parallel, transverse and perpendicular to the build direction). It should be noted that the observed sections were taken from the middle of the deposit. Electron microscopy (SEM), angular selective backscattered (ASB) and Electron backscattered diffraction (EBSD) were used for a detailed analysis. Each section was grounded up to 1,200 grit sandpaper and mirror polished using a 0.04-μm OPS suspension. The Supra 55VP scanning electron microscope performed SEM and ASB imaging at an accelerating voltage of 20 kV. For the EBSD measurements, a FEG Quanta 3-D FEI SEM operating at 20 kV and 8 nA was used. The data acquisition was elaborated by TexSEM Laboratories Inc., software (TSL). Multiple scans covering an area of 1,850 μm × 1,850 μm with a step size of 1.5 μm were executed for the samples of interest. The average confidence index for all measured samples was higher than 0.70. TSL orientation imaging microscopy (OIM) Analysis V6.1 software and the ATEX software were used to perform the post-processing analysis on the EBSD data (Beausir and Fundenberger, 2017). The post-processing of the obtained data was a one-step grain dilatation function with a threshold of 5°.

3. Result

3.1 Mechanical response of the printed 316L SS

A mapping of the mechanical properties with respect to the used processing parameters and the toughness, yield stress and ductility of the heat-treated components is illustrated in Figure 2. For the tensile stress-strain curves of the printed and heat-treated conditions refer the Figure S1(a)–€ and Table S1 in supplementary material and the reference (Khorasani *et al.*, 2021). Here, the 4D colour maps enable a better overview of the impact of processing parameters on the mechanical performance of the printed parts. The variations of the mechanical properties with respect to the processing parameters in Figure 2(a) can be categorised into three characteristic regions: region (I), having the lowest toughness value at lower laser scan speeds and annealing temperatures; region (II), an increase in toughness with the decreasing scanning pattern angle (two saddle points); and region (III) highest toughness for the LB-PBF product at the fastest scan speeds and highest annealing temperatures. It should be noted that the scanning pattern angle does not remarkably influence region (I) toughness values, while its role is significant at higher

Figure 2 The overall view of (a) the LB-PBF scanning parameters and (b) the overall toughness of the LB-PBF 316L SS and (c) the comparison of the uniform elongation and yield strength for various processed 316L SS from Liverani *et al.* (2017), Sun *et al.* (2018), Niendorf *et al.* (2013), Yadollahi *et al.* (2015), Chao *et al.* (2021), Zeng *et al.* (2021), Zhang *et al.* (2020), Carlton *et al.* (2016), Mertens *et al.* (2014), Agrawal *et al.* (2021), Hong *et al.* (2019) and the results obtained in the current work

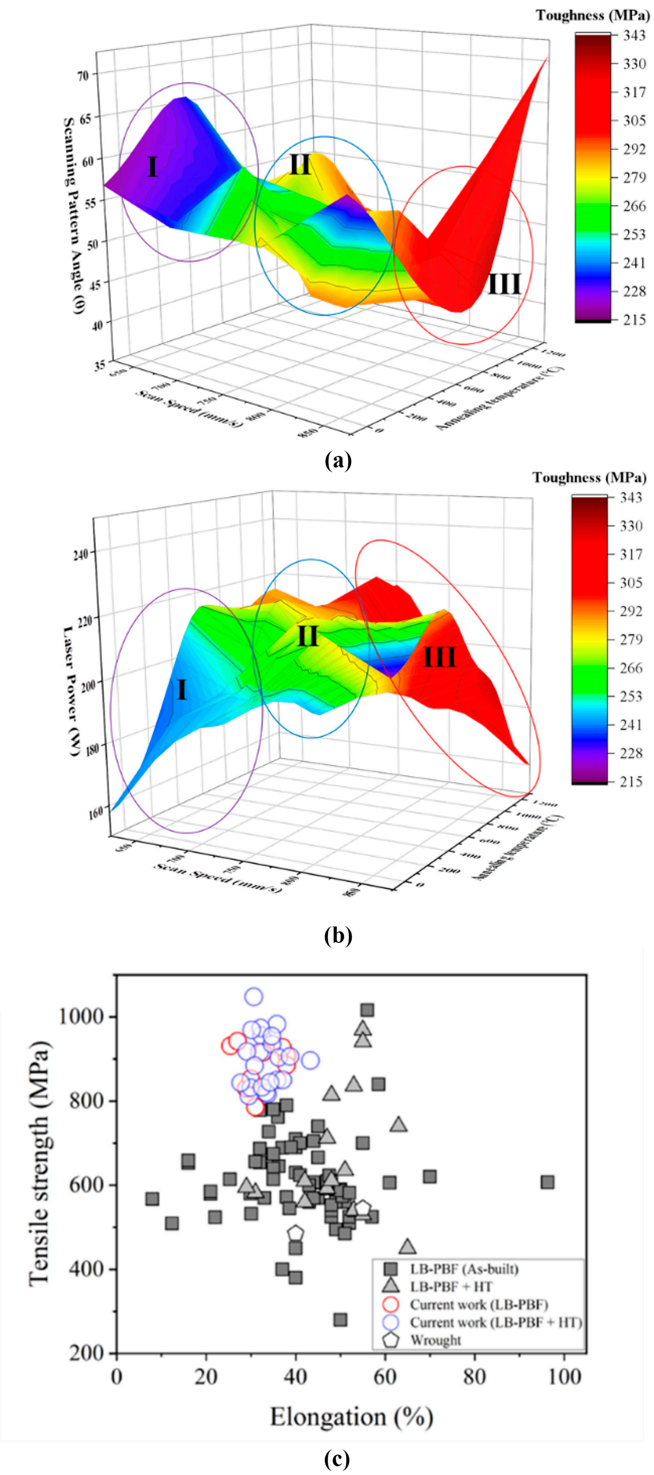

annealing temperatures and faster scan speeds (region III). Similar regions can be considered in Figure 2(b), where the laser power is also considered for its role in the toughness values. The laser power can have different roles as it can both enhance and deteriorate the mechanical properties at low values [i.e. comparing regions I and III in Figure 2(b)]. This means that heat treatment temperature, scanning speed and the scanning pattern angle are crucial factors in optimising the properties of the LB-PBF product. For the sake of comparison, a summary of yield stress versus uniform elongation for various 316L SS, including current work, high-performance materials and conventionally processed materials, is provided in Figure 2(c). It can be observed that tensile strength for the LB-PBF products using the optimised condition can provide a significant improvement in strength and ductility compared with previous attempts using the LB-PBF AM technology. A similar simultaneous increase in strength and ductility has been reported through optimisation of laser power in LB-PBF process (Sun, 2019).

To analyse the experimental results based on the designed processing parameters, the energy density input was measured. The energy density input from Table S1 is estimated according to the following equation (14):

$$E_D = \frac{\eta . P_L}{B_A . v} \tag{1}$$

where P_L is the laser power, ν is the scan speed, η is absorption ratio (0.3 for stainless steel 316L) and B_A is beam area. The calculated values of energy density are presented in the Table S2. It should be noted that the energy density is regarded as a rule of thumb (Prashanth *et al.*, 2017) for evaluating the quality of the built product, namely, the density and mechanical performance. In this regard, melt pool instabilities, such as lack of fusion and void formation, can be avoided when a proper energy density input is selected for the LB-PBF process. In fact, the quality of the built product, namely, the density and mechanical properties, is strongly dependent on the remaining porosity (Gibson *et al.*, 2021). The increase in the build rate requires the highest hatch distance and scan speeds. Therefore, LB-PBF process optimisation needs to tackle the quality of AM products besides increasing the build rate. Figure 3(a) and (b), reveals the as-print build density variations concerning the scanning speed and laser power. The average density of the printed builds is additionally plotted with respect to the energy density (J/mm^3) and the corresponding tensile strength and elongation values [Figure 3(c)]. Here, the lower density for laser powers below 150 W suggests local insufficient energy transfer to the powder particles leading to the formation of porosity and voids in the samples. Such behaviour is reflected by a decrease in tensile strength and elongation values for the tested samples [Figure 3(c)]. For a better observation of the experiment intervals a whisker plot is provided in Figure S2. Therefore, a lower bound of 98.8%-part density is considered for the LB-PBF, meaning that laser powers higher than 175 W can be considered as a suitable range for LB-PBF. These process settings correspond to a volumetric energy density of 6.7–14.7 J/mm^3, within which the specimens achieved the highest tensile strength and elongation. In this window, the condition printed with a 175 W laser power delivered the best

Figure 3 Density variations of LB-PBF concerning (a) hatch distance and scan speed, (b) hatch distance and laser power and (c) energy density versus average relative density, breaking elongation, average max stress and average toughness

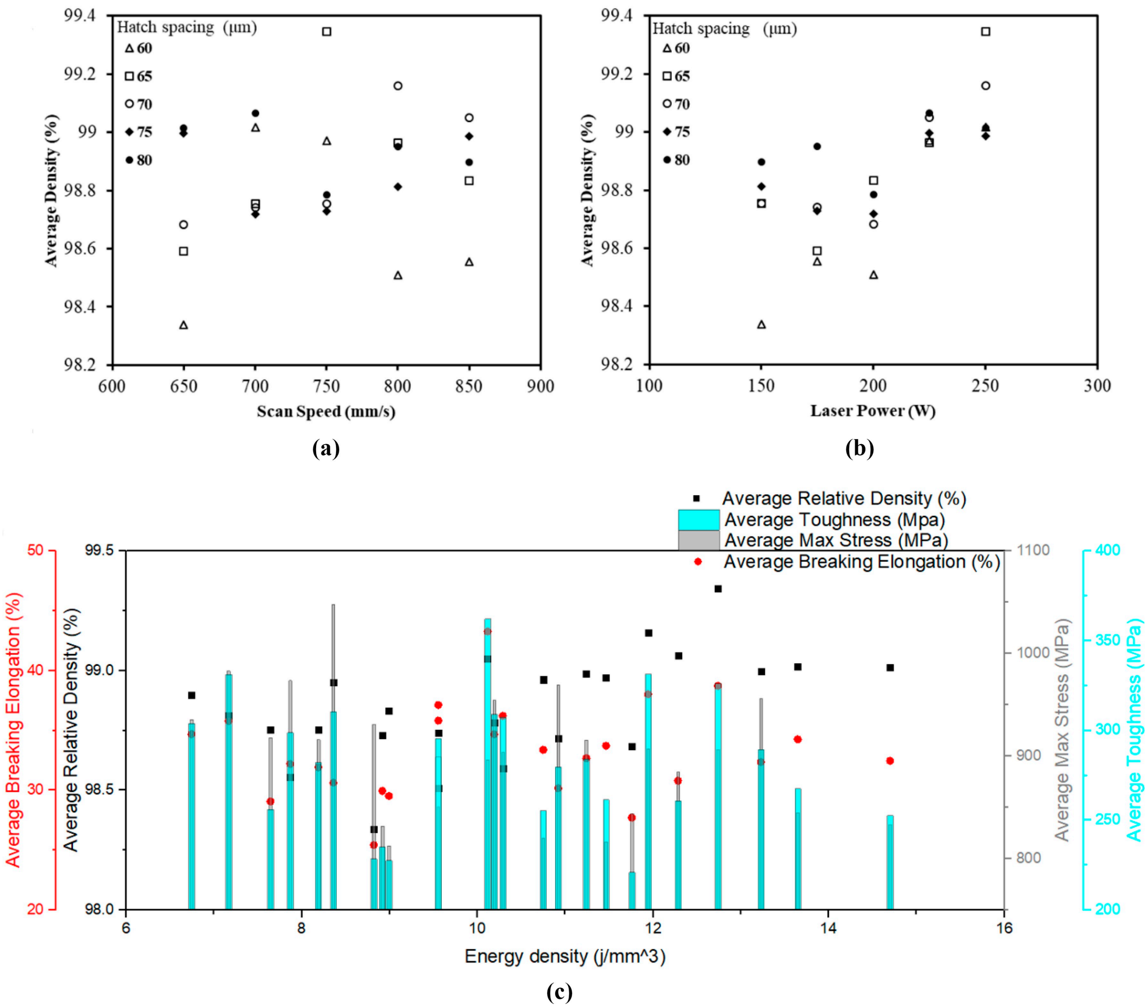

combination of mechanical properties and near-full as-printed density. Accordingly, we selected the 175 W build for detailed analysis to elucidate the origin of the observed property enhancements among all examined conditions.

3.2 Microstructure evolution

3.2.1 The as-built state

Figure 4 shows the SEM images of the LB-PBF 316L SS specimens before the heat treatment at laser power values between 175 and 250 W. The columnar grains were present in all conditions that crossed several melt pool boundaries and can be attributed to the high thermal gradient in the *z*-axis (building direction). As illustrated in Figure 4(a)–(f), the size and morphology of the melt pools in the two samples drastically differed, with different laser power inputs showing smaller melt pool boundaries at higher laser powers. It should be noted that the microstructure of the as-built samples did not represent high internal stress development. This may be associated with the preheating procedure of the substrate and the thermal cycles during the LB-PBF process, resulting in an in-situ annealing of the as-printed product. The microstructure

Figure 4 SEM images representing the melt pool boundaries for the LB-PBF samples at (a) 175, (b) 200 and (c) 250 W laser power. The corresponding angular selective backscattered (ASB) images related to samples printed at (d) 175, (e) 200 and (f) 250 W laser power

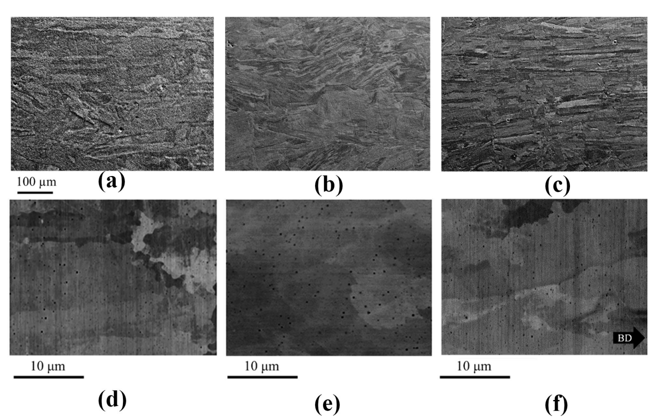

Rapid Prototyping Journal
Volume 32 · Number 11 · 2026 · 146–162

analysis of all the LB-PBF conditions indicated a significant abundance of inclusions that formed within the austenite grains. The inclusion size distribution exhibits a bimodal pattern inside the austenite grain structure, and this pattern remains relatively stable despite modifications in the process parameters. The LB-PBF 316L SS has a greater oxygen concentration compared to the wrought counterpart, mostly because of the excessive input of oxygen during powder atomisation and LB-PBF printing (Chao *et al.*, 2017). This condition can promote the formation of very small oxide inclusions, varying in size from micron to nano, containing high levels of Si, Mn and Cr due to the quick solidification in the LB-PBF process. Formation of these inclusions were previously documented in the LB-PBF process of 316L steels and were demonstrated to be precursors of σ-phase development (Chao *et al.*, 2021; Kurzynowski *et al.*, 2018).

3.2.2 Heat-treated microstructures

Samples manufactured by 175 W laser power were considered for analysing the effects of heat treatment on the microstructure evolution (Figure 5). This is mainly due to the lower energy consumption, higher quality of the fused material (i.e. density and porosity values, Figure 3) and enhanced mechanical properties compared to other LB-PBF samples (Figure 2 and Table S1). The microstructure of the as-printed 316L SS did not undergo any significant changes in the inclusions' characteristics after the stress-relieving treatment at 425°C [Figure 5(a)]. The backscattered electron images displayed these particles as a phase with a dark contrast, primarily found within the austenite grain interior boundaries. Heat treatment at higher temperatures resulted in a slow increase in the size of the inclusions [Figure 5(b)–(e)]. However, the average size is nearly 100 nm for most of the heat treatment conditions. An examination of the inclusion size distribution [Figure 5(f)] shows that the inclusion particles undergo restricted growth as the heat treatment temperatures increase, leading to a bimodal size distribution at 1,050°C [Figure 5(e)].

The EBSD analysis was performed on all three cross-sections (*YZ*, *XZ* and *XY*) of the heat-treated samples at 425°C, 650°C, 870°C and 1,150°C temperatures (Figure 6). Overall, a relatively chaotic configuration of grains consisting of different sizes and shapes is present for both the as-built and heat-treated samples (Figures 4 and 6). The *XZ* and *YZ* sections show a bimodal microstructure having columnar grains across the layers parallel to the build direction (BD) and decorated by fine grain structure along the grain boundaries. An interesting observation is the formation of rhombus-shaped grain morphology consisting of fine and large grains along the *XZ* section in the heat-treated sample. This can be associated with the meander scanning strategy. It is also apparent that the increase in the heat treatment temperature diminished the fine sub-grain structures (i.e. low angle boundaries) and the growth of coarser grains [compare the grain structure in Figure 6(a) with Figure 6(e)]. Heat treatment at the stress-relieving temperature (i.e. 425°C) provides no remarkable changes in the *YZ* cross-section compared to the as-printed microstructure, revealing a similar <101> texture along the build direction. Although a gradual shift in the grain size can be observed for the heat-treated samples at higher temperatures, the microstructure of the YZ cross-section maintains the dominant <101> texture of the as-printed sample. It should be noted that small bands of <100> oriented grains observed for

Figure 5 The angular selective backscattered (ASB) images related to samples printed at 175 W laser power and heat treated at (a) 425°C, (b) 650°C, (c) 870°C, (d)–(e) 1,050°C and (f) the inclusion size distribution under selected conditions

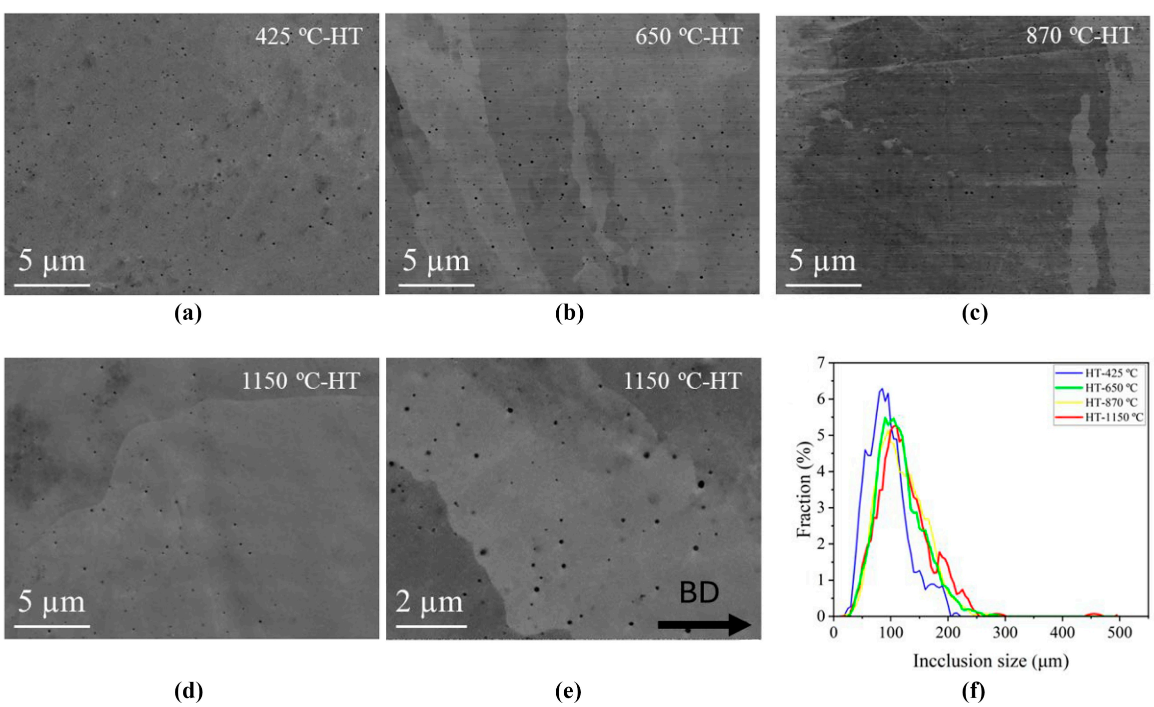

Rapid Prototyping Journal
Volume 32 · Number 11 · 2026 · 146–162

Figure 6 Three-dimensional inverse pole figures of LB-PBFed 316L SS specimens were obtained along the BD for the laser power of 175 in (a) as-built conditions and heat treated at (b) 425°C, (c) 650°C, (d) 870° and (e) 1,150°C

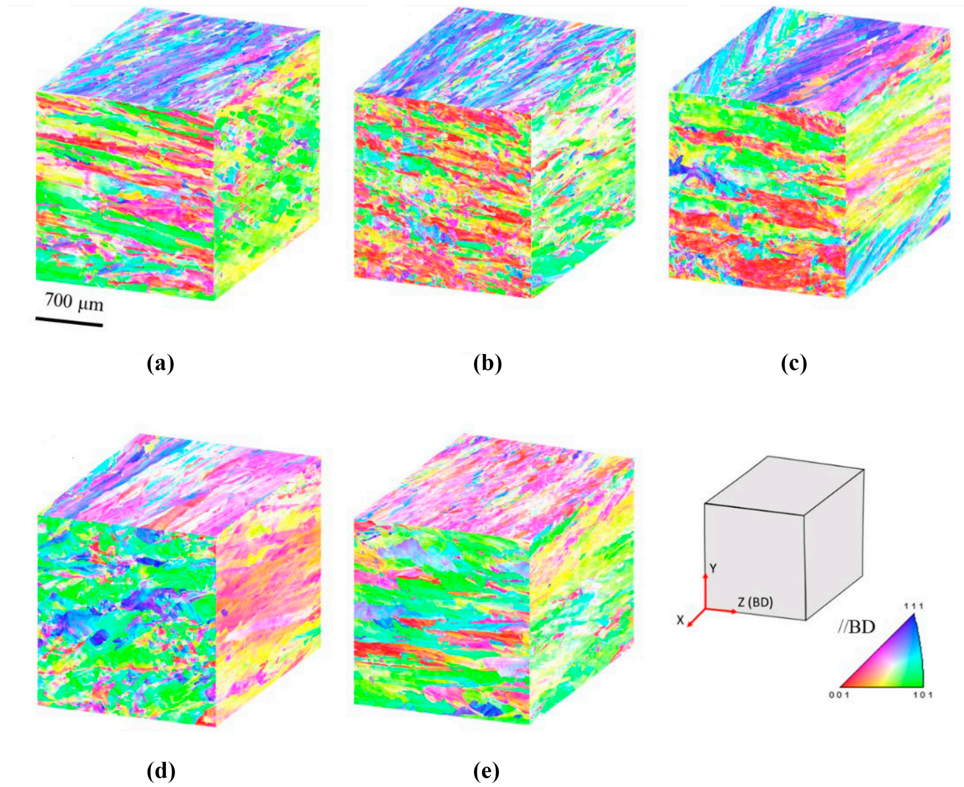

the as-printed samples are still present in all the heat-treated microstructures. The formation of the <100> bands is associated with the preferential growth of the FCC structured material, making a 45° angle with the <101> planes and forming the observed cell inclination in the *XY* cross-sections. The cube texture in the microstructure seems to be diminished with the increase in heat treatment temperature, while the <101> along the BD is strengthened.

The variation of misorientation angle distribution and internal stress development with the heat treatment temperatures is presented in Figure 7. Upon heat treatment, the columnar austenitic grain morphology remained similar in the as-fabricated microstructure [Figure 6(a)] and heat-treated ones [Figure 6(b)–(e)], while the fraction of low angle boundaries reduced significantly with the increase in heat treatment temperature [Figure 7(a)]. The reduction in the number fraction of low-angle boundaries (i.e. $5^\circ < \theta < 15^\circ$) is followed by an increase in the high-angle boundaries at higher heat treatment temperatures. This may hint at the occurrence of grain boundary migration and recrystallisation at heat treatment temperatures higher than 425°C (i.e. 650, 870 and 1,150°C). It should be noted that the Σ3 (60°/<111>) boundary fraction is extremely limited in the as-built state while it increases and reaches its maximum at 650°C condition [Figure 7(a)]. It can be observed that the formation of Σ3 is not significantly affected by the heat treatment of the samples as the temperature increases to 1,150°C.

A qualitative understanding of the residual stress distribution within the microstructure can be observed in the kernel average misorientation (KAM) maps in Figure 7(b). KAM maps are generated by averaging the misorientation between a centre pixel (the kernel) and its neighbouring pixels. Then, the generated KAM map exhibits local orientation variations, which are associated with distortions within the lattice structure (i.e. as a result of dislocation accumulation or thermal stresses). The two KAM maps of samples in the heat-treated samples at 425°C and 1,150°C conditions [Figure 7(b) and (c)] reveal that the part heat-treated at 425°C has a higher residual strain compared with the sample heat-treated at 1,150°C. This reduction in local lattice distortion, inferred from KAM analysis, follows the decreasing fraction of low-angle boundaries with increasing heat-treatment temperature [Figure 7(a)]. The higher the heat treatment temperature, the higher the kinetics of grain boundary migration, which reduces the degree of dislocations and strain within the as-built material.

3.2.3 *LB-PBF microstructure stability*

The assessment of the microstructure and mechanical stability was conducted by considering the effect of annealing temperature on the grain size and tensile properties. The tensile strength increases with heat treatment up to 650°C and then decreases for higher temperatures. For the lower heat treatment regime (<650°C) the grain size changes around $\pm 5\,\mu$m of the as-built microstructure, while for higher temperatures it goes as high as $+15\,\mu$m for 1,150°C. This increase in the grain size is followed by a reduction in the tensile strength to 910 and 850 MPa for the 870°C and 1,150°C heat treatment temperatures,

Figure 7 (a) The misorientation angle distribution for different heat treatment routines, (b) the KAM maps corresponding to the heat-treated samples at 425°C and (c) 1,150°C. Here, Kernel maps were calculated concerning all neighbours at 500 nm distance, excluding values above 5°

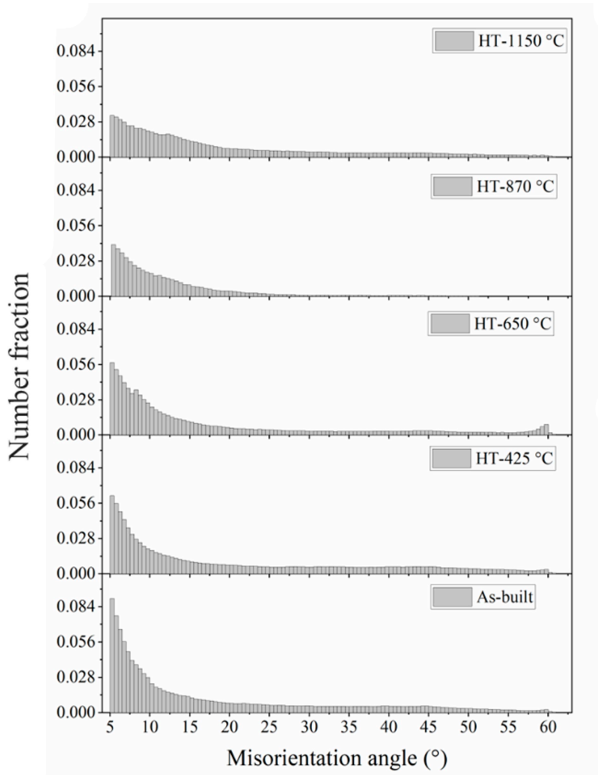

(a)

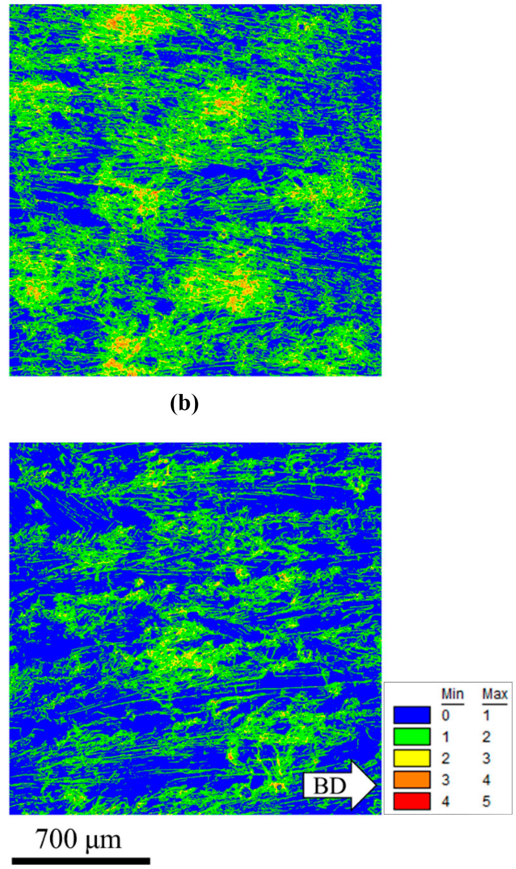

(b)

(c)

Figure 8 Comparison of the tensile strength and grain size of LB-PBF 316L SS samples in the as-built and heat-treated conditions

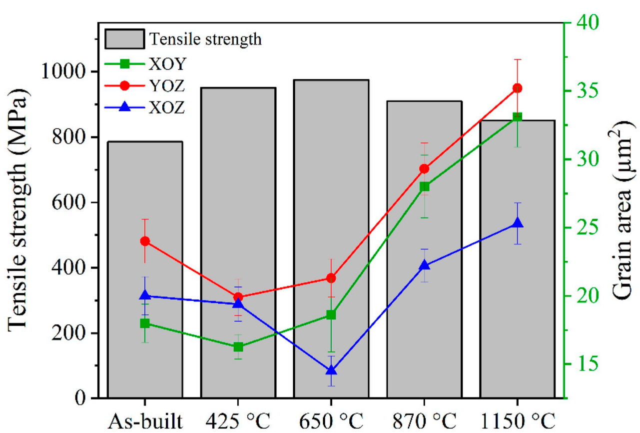

respectively. Preferential growth of the grains was also witnessed within different sections of the heat-treated samples (Figure 8). As the heat treatment temperature increases, grains along the *XZ* section tend to grow slower than those along the *XY* or *YZ* area, further confirming the preferential growth along <101> occurring during the heat treatment procedure.

3.2.4 LB-PBF texture evolution

The crystallographic texture development in the build direction is presented in Figure 9. The sample in the as-built condition reveals a weak texture in the (110) and (100) pole figures [Figure 9(a)]. This can be associated with the variation of the scan direction, which influences the heat flow, the complexity of the grain structure and therefore lower overall texture intensity. Previous studies on various scan rotations during LB-PBF also showed a significantly lower overall intensity than the sample produced without scan rotation (Wei *et al.*, 2015; Leicht *et al.*, 2020). The employment of heat treatment at 425°C showed minimal influence on the overall texture intensity [Figure 9(a) and (b)]. As the heat treatment temperature increases to 875°C and 1,150°C, the overall texture shows a preference within the (110) poles [Figures 9(c) and (d)]. It seems that the weak as-printed texture becomes dominant with the increase in the heat treatment temperatures. The heat treatment at 1,150°C had the highest intensity, with an intensity of 9.6 and 5.61 times random for (100) and (110) poles [Figure 9(d)]. Observing the EBSD maps and the pole figures, it is apparent that the random orientation (observed in the colour maps of the as-built microstructures, Figure 9(a) are promoting the weak texture intensity for the as-built, while the preferential grain growth along the < 101> direction results in an increased intensity for the heat-treated samples at 875°C

Figure 9 Texture development in the *x*-transverse direction (TD) and *y*-build direction plane is represented using (100) and (110) pole figures for the laser power of 175 W and different heat treatment conditions: (a) as-built, (b) 425°C, (c) 870°C and (d) 1,150°C

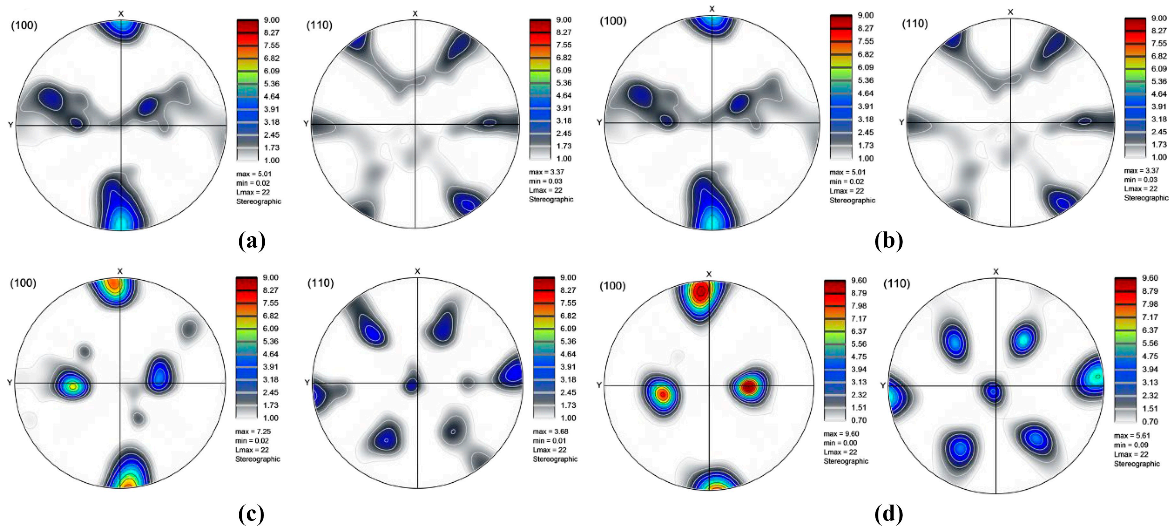

and 1,150°C. The preferential grain growth during the heat treatment has been previously reported in the literature (Salman *et al.*, 2019; La Fé-Perdomo *et al.*, 2023).

4. Discussion

It was observed that the employment of different LB-PBF parameters along with scanning strategy and different heat treatment procedures resulted in a significant difference in the grain size and morphology. In parallel, the texture has been strongly influenced by the substructure developed during the heat treatment procedure, resulting in a strong cubic texture for high-temperature treatments while showing random properties in the as-built condition. Such characteristic microstructures significantly improved the mechanical properties related to the grain size effect and dominant deformation mechanism associated with each developed microstructure. These will be discussed in the following.

4.1 The role of grain structure on the mechanical properties

The mechanical property window presented in Figure S1 showed that the material could have ultimate tensile strength (UTS) values as high as 950 MPa for the laser power of 175 W being heat treated at 425–870°C. Compared with the as-built condition, the mechanical properties after the heat treatment show a significant increase which can be attributed to activation of different strengthening mechanisms naming the grain size strengthening (σ_{GB}), solid solution strengthening (σ_{SS}) and dislocation strengthening (σ_{Dis}). To define the role of each, the rule of the mixture can be elaborated for each condition:

$$\sigma = \sigma_0 + \sigma_{GB} + \sigma_{SS} + \sigma_{Dis} \tag{2}$$

where σ_0 is the constant value, which is considered to be approximately 15 MPa as indicated by Nabarro for the austenitic iron (Nabarro, 1997). The grain size values for the material after the heat treatment procedure are relatively higher when compared with the as-built condition (Dwivedi *et al.*, 2024). However, the change in the grain size is not accompanied by the improved mechanical properties of the as-built material. The lower mechanical properties can be influenced by the lack of fusion defects in the as-built material, which are reduced through heat treatment (Malik *et al.*, 2024). However, a deeper understanding of each strengthening factor's role is required. For different heat treatment regimens, the change in the grain size shows a meaningful trend with the strength of the material; therefore, the grain boundary strengthening (σ_{GB}) can be measured using the modified Hall-Petch relation for the materials having bimodal microstructures (i.e. different grain sizes):

$$\sigma_{GB} = f_{small}\frac{k_y}{\sqrt{d_{small}}} + f_{large}\frac{k_y}{\sqrt{d_{large}}} \tag{3}$$

where k_y is the strengthening coefficient taken as 452 MPa/$\mu m^{-1/2}$ (Huang *et al.*, 2011), moreover, f_{small}, f_{large} and d_{small}, d_{large} in equation (3) are the area fractions and average grain sizes of the small and large grains, respectively; and values of them have been provided in Table 3. In this regard, the yield strength variations associated with the grain-size refinement are measured and presented in Table 3.

The contribution of solid solution strengthening to the yield strength of steels has been previously studied by the Van-Bohemen expression and was calculated as 96.6 MPa for the 316L austenitic steel (Van Bohemen, 2018). The Si-rich nanoparticles has been also observed in previous research studies showing a significant contribution to the yield strength of different grades of steels (Cui *et al.*, 2021; Eres-Castellanos *et al.*, 2020; Kusakin *et al.*, 2017). It should be noted that while we do not quantify these nano-inclusions at TEM scale here, similar Si/Mn/Cr-rich oxides and their qualitative effects have been observed and discussed in prior LPBF-316L studies and showed that their contribution is limited to 10–15 MPa in 316L stainless steels (Van Bohemen, 2018; Behjat *et al.*, 2024). Therefore, this has not been considered significant in this study.

Table 3 The strengthening components of the LB-PBF 316L and the estimated yield strength (yest) compared to the experimental yield strength

Condition/Temperature	f_{small}	f_{large}	d_{small}	d_{large}	σ_0 (MPa)	σ_{ss} (MPa)	σ_{GB} (MPa)	σ_{Dis} (MPa)	$\sigma_{y_{est}}$ (MPa)	$\sigma_{y_{exp}}$ (MPa)
As-built	0.1	0.9	4.6	38	15	96.6	87.06628	366.7	565.4	627
425°C	0.13	0.87	5	45	15	96.6	84.89903	333.49	530.0	772
650°C	0.22	0.78	7	39	15	96.6	94.03957	301.14	506.8	816
870°C	0.22	0.78	8.4	68	15	96.6	77.06424	271.12	459.8	684
1,150°C	0.28	0.72	9.2	73	15	96.6	79.81547	264.86	456.3	649

The formation of geometrically necessary and statistically stored dislocations can also contribute to the overall strength of the printed alloy. Therefore, the term of the σ_{Dis} can be attributed to the strengthening effect obtained from dislocation cell structures within the printed material. This term can be easily obtained by calculating the dislocation density from the geometrically necessary dislocation (GND) maps of the EBSD measurements. The calculated dislocation densities for the as-built and heat-treated samples for 475°C, 650°C, 870°C and 1,150°C are 7.8×10^{14}, 6.5×10^{14}, 5.3×10^{14}, 4.3×10^{14} and 4.1×10^{14}, respectively. The GND maps of the LB-PBF samples are provided in Figure 10(a)–(d). The GND density was calculated using the ATEX software function developed by Agrawal *et al.* (2021). The portion of the dislocation strengthening can be calculated based on the following equation:

$$\sigma_{GB} = M\alpha Gb\sqrt{\rho}, \tag{4}$$

where the M, α, G and b are Taylor factors (i.e. 2.98–3.08 according to the EBSD maps), the magnitude of Burgers vector ($b=0.2546$ nm in austenitic steels) and shear modulus (i.e. 73 GPa), respectively (Yin *et al.*, 2019). As shown in Table 3, the obtained σ_{Dis} from the dislocation strengthening used in the as-built condition is 366.7 MPa and decreases from 264.86 MPa with increasing annealing temperature. As observed, the measured yield strength deviates from the experimental results, which can be attributed to dynamic factors such as the formed precipitates and texture during straining. In this regard, the each will be evaluated for further analysis.

4.2 The role of texture on the mechanical properties

Along with the strengthening achieved through the Hall–Petch grain boundary, the twin boundary formation during the straining, mainly considered as the 60°/<111> misorientation, can significantly affect the strengthening of the FCC structured alloys. This can be associated with the unique characteristics of the LB-PBF material resulting in numerous low and high-angle grain boundaries, which contribute to enhanced ductility and strength (Salman *et al.*, 2019; Leff, 2013; Jørgensen *et al.*, 2017; Chinh *et al.*, 2006; Fri *et al.*, 2023). To investigate the observed discrepancies between the heat treatment procedure and the printed material's yield strength, the microstructure developed within the materials after the tensile tests were analysed and depicted in Figure 11(a) and (b). Overall, the high strain hardening rate observed in the printed samples is primarily associated with the occurrence of twinning in the FCC material. The difference in the propensity of twinning in the annealed samples can be related to the texture promoting the <112> twinning samples (Kamath *et al.*, 2014; Yan *et al.*, 2014). Considering the Taylor factor maps mentioned for the slip and twinning happening during uniaxial straining, the <111> and <110> orientations are more favourable for twinning rather than the <100> orientations (Hosford, 1993; Farabi *et al.*, 2019).

The twinning propensity can be observed in Figure 11, where the microstructure of the printed samples was heat-treated to 650°C. Here, the formation of the twins is more prominent along the <111> orientated grains than the <100> grain, which had almost zero twins formed. Besides, the critical nucleation of twins follows the Hall–Petch relationship as the higher yield stress results in higher critical stress for twinning (Meyers and Chawla, 2008). The presence of the cellular structure, which imposes a high density of dislocations, is crucial in suppressing the mechanical twinning initiation. Therefore, for the as-built sample, the higher fraction of low-angle boundaries may resemble a higher resistance for twinning, restricting the nucleation and growth of the deformation twins. As the annealing removes the dislocation density in the sample, a higher propensity for twinning during the straining is expected

Figure 10 GND maps corresponding to the IPF maps provided in Figure 7 for (a) as-built and heat-treated samples at (b) 425°C, (c) 870°C and (d) 1,150°C

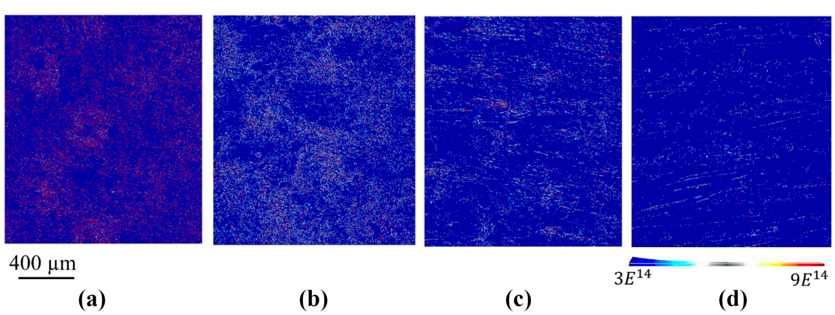

Figure 11 The relative distribution of deformation twin boundaries in various oriented austenite variants in (a) as built and (b) heat treated at 650°C samples

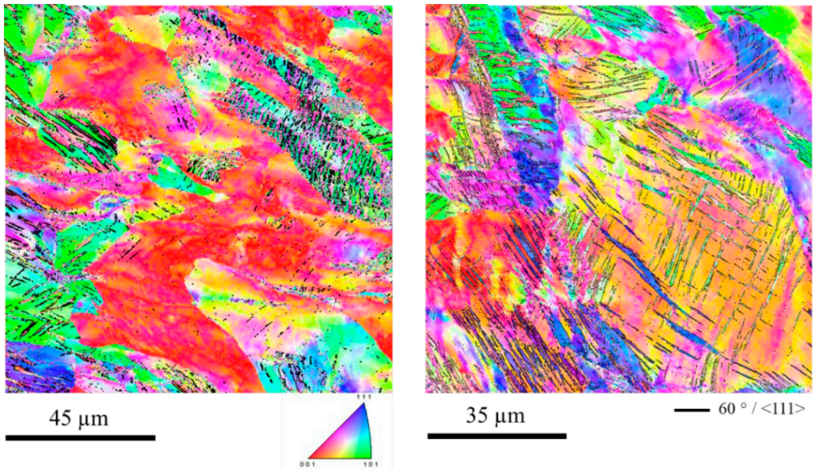

(Hong *et al.*, 2019). On the other hand, the {111} <110> dislocation slip also occurs for the low stacking fault energy metals at low deformation levels. It is well known that the occurrence of slip can actively reorient the unstable orientations towards the <111> and <100> orientations (Hirsch and Lucke, 1988). This results in a continuous rotation of grains in the low-texture grains towards the easy-to-twin orientations for the annealed samples at lower than 870°C. A continuous region of twin boundaries will tend to form along the dislocation paths with the increased strain levels leading to a dynamic Hall–Petch effect (Grässel *et al.*, 2000).

As observed in Figure 12(a) and (b) the formation of deformation twins can divide the microstructure into <5μm regions which can actively inhibit movement of dislocations

Figure 12 (a) and (b) back-scattered electron images of heat treated at 650°C samples. Fractography of the 316L SS in (c) and (e) as-printed and (d) and (f) after heat treatment at 650°C

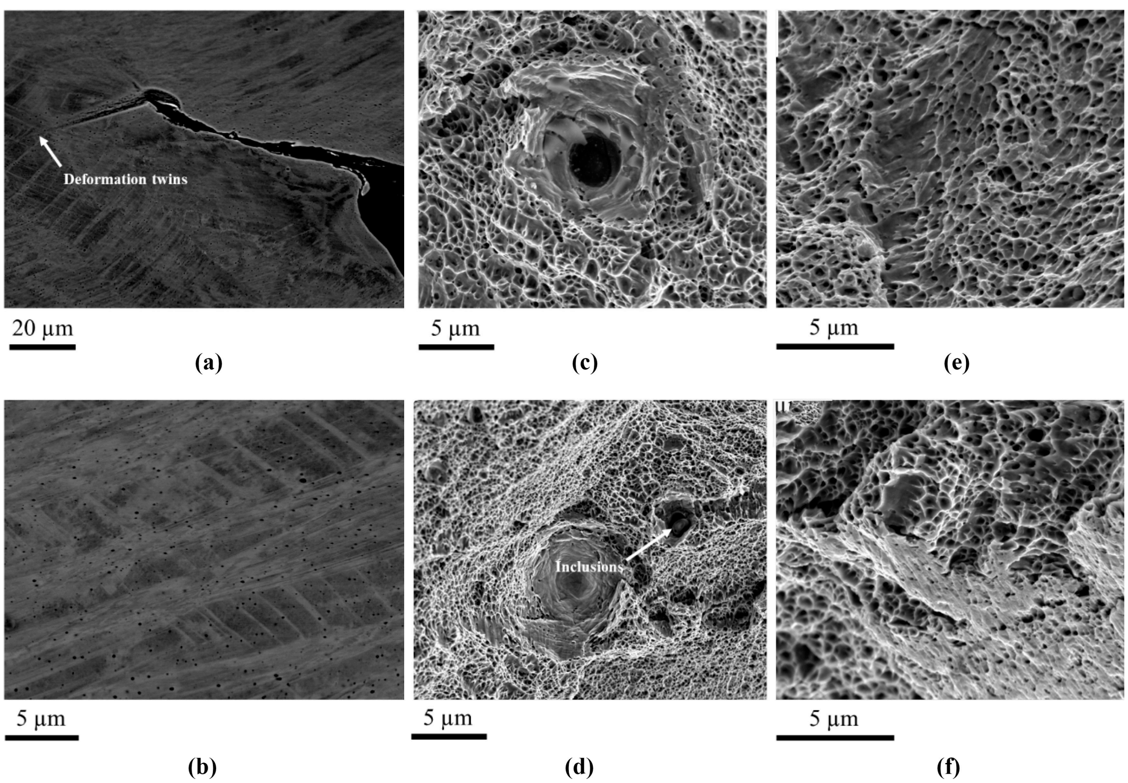

and or micro cracks within the printed sample. This ultimately means that heat-treated samples with <101> texture provide a higher potential for achieving a higher strength and fracture strain combination. However, it should be noted that the analysis of tensile fracture surfaces showed the existence of small-sized particles near the small dimples at the fracture surface of as-built 316L SS [Figure 12(c) and (e)]. In contrast, micron-size particles were observed in the material heat treated at 650°C [Figure 12(d) and (f)]. When subjected to tensile deformation, the observed inclusions can lead to local stress concentration and act a suitable region for the formation of voids at austenite grain boundaries which can result in the reduced ductility observed in the 316L SS samples.

4.3 A brief overview on LB-PBF optimisation advantages of 316L SS

The material properties of additively manufactured components are significantly affected by grain size, texture and the size, distribution and volume fraction of porosity (Ronneberg *et al.*, 2020; Röttger *et al.*, 2016; Carlton *et al.*, 2016; Kazemipour *et al.*, 2019) . The observed fraction is relatively low in the current LB-PBF 316L manufactured parts (i.e. less than 1% for the optimum conditions) and was unaltered by the applied heat treatments (Figure 3) (Tascioglu *et al.*, 2020). Thus, the ductility and strength achieved in the current work can be mainly related to other factors, including coarsening of austenite grains and inclusions or the formation of secondary phases or precipitates and the extent of dislocation density within the built samples. In this study, the optimised condition (175 W) generated a refined austenitic grain, limited porosity and a strong {101} <111> texture aligned along the build direction. Such texture evolution results from directional solidification under steep thermal gradients and cyclic reheating, which stabilises columnar grains and restricts the formation of σ phase. The resultant structure provides improved tensile strength and uniform elongation due to the combined effects of grain refinement, reduced defect density and homogenised elemental distribution (Hsieh and Wu, 2012). Such microstructure characteristics in this study show superior mechanical strength when compared to previous reports on additive manufacturing of 316L stainless steels [i.e. refer to Figure 2(c)] and even duplex stainless steels (Chao *et al.*, 2021; Tasan *et al.*, 2015). However, this combination not only forms a foundation for mechanical performance but also enables improved corrosion performance, since both parameters are strongly governed by grain boundary characteristics and inclusion characteristics.

To achieve optimal mechanical performance from the printed 316L SS in its operational state, it is crucial to select appropriate process parameters and heat treatment procedures (such as stress-relieving or solution treatment) based on the desired yield strength, ultimate tensile strength, ductility and work hardening capability (Greco *et al.*, 2024). Optimising the LB-PBF process parameters revealed that using the meander pattern strategy with a laser power of 175 W and a range of pattern angles, hatch spacing and scanning speeds yields the best microstructures for post-heat treatment routines. The stress-relieving treatment at a temperature of 400°C mostly impacts the yielding strength, whereas the UTS and ductility are minimally affected. At a temperature of 650°C, there is a higher degree of stress relief, as well as an associated increase in elongation, yield strength (YS) and UTS values. This phenomenon has been attributed to the existence of inclusions, as seen in Figures 4 and 5. By increasing the heat treatment temperature to 875°C and 1,150°C, the UTS values gradually decrease, indicating the importance of the coarsening of inclusions. However, achieving a fully stress-relieved state leads to an improvement in the elongation values. It is important to mention that subjecting a material to long-term stress relief and solution treatment at temperatures ranging from 650 to 1,100°C and higher can lead to a decrease in yield strength, tensile elongation and corrosion resistance (Zhou *et al.*, 2020; Kong *et al.*, 2018). This is mostly caused by recrystallisation, grain growth and the enlargement of inclusions.

Besides the mechanical performance, the corrosion resistance of LB-PBF 316L stainless steel is intrinsically governed by its unique non-equilibrium microstructure, which has significantly different characteristics from its wrought counterpart (Haghdadi *et al.*, 2021). In this study the as-built microstructure, characterised by a cellular sub-grain structure bounded by a network of low angle grain boundary (LAGBs) with a limited fraction of Σ3 annealing twins, can be inherently resistant to intergranular corrosion. This is not just a correlation, as it is a direct consequence of the limited diffusion pathways along these low-energy interfaces. It should be noted that the beneficial effect of low-angle boundaries in the as-built state is twofold. They are associated with lower stored strain energy compared to random high-angle boundaries and the cellular boundaries themselves are often enriched with Mo and Cr oxides, enhancing passivation (Laleh *et al.*, 2021; Kong *et al.*, 2024). The effect of heat treatment is complex and depends on the temperature regime. The observed decrease in low-angle boundary density during annealing in the 650–870°C range is a signature of recovery and recrystallisation. While this can diminish the dislocation-driven micro-galvanic heterogeneities, it also breaks down the cellular structure and eliminates the beneficial Mo/Cr-enriched sub-grain boundaries (Laleh *et al.*, 2021). Furthermore, exposure in this intermediate temperature range is where the risk of detrimental phase precipitation (e.g. $M_{23}C_6$ carbides, σ phase) is highest (Laleh *et al.*, 2021; Ni *et al.*, 2018). Therefore, its advantages are dependent on the heat treatment successfully relieving residual stress without stimulating the precipitation at random high-angle boundaries.

The crystallographic texture also plays a decisive role in pitting resistance. The dissolution kinetics of austenitic stainless steels are highly orientation dependent. Close-packed {111} planes, with their higher atomic coordination and density, promote the formation of a more stable and protective passive film, leading to slower dissolution rates (Wei *et al.*, 2022; Ma *et al.*, 2025). In contrast, the more open {100} planes are inherently less stable and more prone to film breakdown. The <110> and <101> texture components typically developed in optimised LPBF 316L, often associated with the melt pool geometry and competitive grain growth, effectively increase the probability of {111}-oriented grains intersecting the exposed surface. This texture strengthening, by favouring the exposure of corrosion-resistant crystallographic planes, directly contributes to a higher pitting potential compared to a

Rapid Prototyping Journal
Volume 32 · Number 11 · 2026 · 146–162

strongly <100>-fibered texture common in some other processing routes. Together, these characteristics promote a microstructure that can potentially enhance both mechanical and corrosion resistance for AM 316L alloys.

5. Conclusion

This study presents an algorithm that effectively determines the best LB-PBF processing and post-heat treatment parameters for producing 316L stainless steels with reduced energy consumption and improved characteristics. The Taguchi design of the experiment was elaborated to reduce the time and cost of the experiments for identifying a wide range of LB-PBF process parameters. The LB-PBF was conducted in a range of 150–250 W laser power with changing scanning speeds and angles. Then, using various microstructure characterisation techniques, the role of heat treatment on the mechanical at the temperature range of 425–1,150°C was investigated. The main finding of the current study can be summarised as follows:

- The multi-objective optimisation of the suitable LB-PBF revealed the 175 W as the optimised region with the highest mechanical properties. The obtained experimental results displayed low energy densities of 6.7 J/m^3 to 14.7 J/m^3 within the laser power range and were capable of producing parts with a relative mass density of 98.8% or higher.
- Heat treatment was shown to have the most decisive influence on the mechanical properties compared to the process parameters. The maximum tensile properties were achieved for laser powers of 175 and heat treatment at 870°C with tensile strength up to 970 MPa and elongations of approximately 32%, while these values were between 700 and 900 MPa and 20%–30% for the as-printed parts, respectively.
- The microstructure of heat-treated samples had a complex grain configuration with different sizes and shapes. The heat treatment resulted in grain growth from approximately 20 μm up to approximately 45 μm for temperatures of 425°C and 1,150°C, respectively. However, the grains tend to grow at various rates at higher heat treatment temperatures (i.e. > 650°C) leading to anisotropic microstructures on different sections of the printed material.
- The increase in the heat treatment temperature resulted in the preferential growth of <110> grains and the disappearance of <100> grains in the as-built condition. This led to the dominance of <110> orientations at higher heat treatment temperatures and subsequent preference for mechanical twinning during tensile straining.
- The analysis of microstructure using the Hall-Petch relationship shows that dislocation strengthening and grain boundary strengthening had a major role in the mechanical properties of the as-built material. However, heat treatment at temperatures higher than 650°C and grain reorientation to <110> components promoted mechanical twinning and dynamic Hall–Petch effect, increasing printed material's strength and ductility.

References

Agrawal, P., *et al.* (2021), "Processing-structure-property correlation in additive friction stir deposited Ti-6Al-4V alloy from recycled metal chips", *Additive Manufacturing*, Vol. 47, p. 102259.

Andreau, O., *et al.* (2019), "Texture control of 316L parts by modulation of the melt Pool morphology in selective laser melting", *Journal of Materials Processing Technology*, Vol. 264, pp. 21-31.

ASTM, I. (2016),*ASTM E8/E8M-16a: standard Test Methods for Tension Testing of Metallic Materials*, ASTM International, West Conshohocken, PA, USA.

Bahl, S., *et al.* (2019), "Non-equilibrium microstructure, crystallographic texture and morphological texture synergistically result in unusual mechanical properties of 3D printed 316L stainless steel", *Additive Manufacturing*, Vol. 28, pp. 65-77.

Bajaj, P., Hariharan, A., Kini, A., Kürnsteiner, P., Raabe, D., Jägle, E.A., *et al.* (2020), "Steels in additive manufacturing: a review of their microstructure and properties", *Materials Science and Engineering: A*, Vol. 772, p. 138633.

Beausir, B. and Fundenberger, J. (2017), "Analysis tools for electron and X-ray diffraction.", *ATEX-software*, Vol. 201 No. 7.

Behjat, A., *et al.* (2024), "Laser powder bed fusion in situ alloying of AISI 316L-2.5% Cu alloy: microstructure and mechanical properties evolution", *Progress in Additive Manufacturing*, Vol. 9 No. 6, pp. 1-9.

Carlton, H.D., *et al.* (2016), "Damage evolution and failure mechanisms in additively manufactured stainless steel", *Materials Science and Engineering: A*, Vol. 651, pp. 406-414.

Chao, Q., *et al.* (2017), "On the enhanced corrosion resistance of a selective laser melted austenitic stainless steel", *Scripta Materialia*, Vol. 141, pp. 94-98.

Chao, Q., *et al.* (2021), "The effect of post-processing heat treatment on the microstructure, residual stress and mechanical properties of selective laser melted 316L stainless steel", *Materials Science and Engineering: A*, Vol. 821, p. 141611.

Chen, X., *et al.* (2018), "Effect of heat treatment on microstructure, mechanical and corrosion properties of austenitic stainless steel 316L using arc additive manufacturing", *Materials Science and Engineering: A*, Vol. 715, pp. 307-314.

Cherry, J., *et al.* (2015), "Investigation into the effect of process parameters on microstructural and physical properties of 316L stainless steel parts by selective laser melting", *The International Journal of Advanced Manufacturing Technology*, Vol. 76 Nos 5-8, pp. 869-879.

Chinh, N.Q., *et al.* (2006), "Experimental evidence for grain-boundary sliding in ultrafine-grained aluminum processed by severe plastic deformation", *Advanced Materials*, Vol. 18 No. 1, pp. 34-39.

Cui, L., *et al.* (2021), "Revealing relationships between microstructure and hardening nature of additively manufactured 316L stainless steel", *Materials & Design*, Vol. 198, p. 109385.

DebRoy, T., *et al.* (2018), "Additive manufacturing of metallic components–process, structure and properties", *Progress in Materials Science*, Vol. 92, pp. 112-224.

Dinda, G., Dasgupta, A. and Mazumder, J. (2012), "Texture control during laser deposition of nickel-based superalloy", *Scripta Materialia*, Vol. 67 No. 5, pp. 503-506.

Dwivedi, A., *et al.* (2024), "Microstructure and mechanical properties at elevated temperatures of as-built and heat-treated Inconel 718 produced through laser powder bed fusion processes", *Rapid Prototyping Journal*, Vol. 31 No. 3.

Ebling, H. and Scheil, M. (1965), "Time-temperature-sensitization (TTS) diagrams for types 347, 304L, and 316L stainless steels", in *Advances in the Technology of Stainless Steels and Related Alloys*, ASTM International, West Conshohocken, PA.

Eres-Castellanos, A., *et al.* (2020), "An integrated-model for austenite yield strength considering the influence of temperature and strain rate in lean steels", *Materials & Design*, Vol. 188, p. 108435.

Farabi, E., *et al.* (2019), "Microstructural evolution and mechanical properties of accumulative back extruded duplex (α+ β) brass", *Materials Characterization*, Vol. 152, pp. 101-114.

Fri, K., *et al.* (2023), "Experimental investigation of the effects of processing parameters and heat treatment on SS 316L manufactured by laser powder bed fusion", *Progress in Additive Manufacturing*, Vol. 9 No. 6, pp. 1-23.

Gibson, I., Rosen, D., Stucker, B., Khorasani, A., Rosen, D., Stucker, B. and Khorasani, M. (2021), *Additive Manufacturing Technologies*, Springer, Cham, Switzerland.

Grässel, O., *et al.* (2000), "High strength Fe–Mn–(Al, Si) TRIP/TWIP steels development – properties – application", *International Journal of Plasticity*, Vol. 16 Nos 10-11, pp. 1391-1409.

Greco, A., Russo, M.B. and Gerbino, S. (2024), "Simultaneous impact of build orientation on mechanical properties, geometrical measurements and surface roughness in material extrusion manufacturing", *Rapid Prototyping Journal*, Vol. 31 No. 11.

Haghdadi, N., *et al.* (2021), "Additive manufacturing of steels: a review of achievements and challenges", *Journal of Materials Science*, Vol. 56 No. 1, pp. 64-107.

Heeling, T. and Wegener, K. (2018), "The effect of multi-beam strategies on selective laser melting of stainless steel 316L", *Additive Manufacturing*, Vol. 22, pp. 334-342.

Hirsch, J. and Lucke, K. (1988), *Mechanism of Deformation and Development of Rolling Textures in Polycrystalline F. C. C. Metals. I. Description of Rolling Texture Development in Homogeneous CuZn Alloys. Acta Metall*, Vol. 36 No. 11, pp. 2863-2882.

Hong, Y., *et al.* (2019), "Formation of strain-induced martensite in selective laser melting austenitic stainless steel", *Materials Science and Engineering: A*, Vols 740-741, pp. 420-426.

Hosford, W.F. (1993),*The Mechanics of Crystals and Textured Polycrystals*, Oxford University Press, New York, NY.

Hsieh, C.-C. and Wu, W. (2012), "Overview of intermetallic sigma (?) phase precipitation in stainless steels", *ISRN Metallurgy*, Vol. 2012.

Huang, C., *et al.* (2011), "Mechanical behaviors of ultrafine-grained 301 austenitic stainless steel produced by equal-channel angular pressing", *Metallurgical and Materials Transactions A*, Vol. 42 No. 7, pp. 2061-2071.

Jørgensen, H., Baadsgaard, K. and Klindt, M.P. (2017), "Beyond flexicurity: the shift towards work-first and its implications for street-level work in the Danish employment system", *Social Work and Research in Advanced Welfare States*, pp. 47-60.

Kamath, C., *et al.* (2014), "Density of additively-manufactured, 316L SS parts using laser powder-bed fusion at powers up to 400 W", *The International Journal of Advanced Manufacturing Technology*, Vol. 74 Nos 1-4, pp. 65-78.

Kazemipour, M., *et al.* (2019), "Microstructure and corrosion characteristics of selective laser-melted 316L stainless steel: the impact of process-induced porosities", *JOM*, Vol. 71 No. 9, pp. 3230-3240.

Khorasani, M., *et al.* (2021), "On the role of process parameters on meltpool temperature and tensile properties of stainless steel 316L produced by powder bed fusion", *Journal of Materials Research and Technology*, Vol. 12, pp. 2438-2452.

Kok, Y., *et al.* (2018), "Anisotropy and heterogeneity of microstructure and mechanical properties in metal additive manufacturing: a critical review", *Materials & Design*, Vol. 139, pp. 565-586.

Kong, D., *et al.* (2024), "Elemental decoration design with metastable cellular substructures for additively manufactured high-strength and high-corrosion resistant austenitic stainless steel", *Corrosion Communications*, Vol. 13, pp. 17-26.

Kong, D., *et al.* (2018), "Heat treatment effect on the microstructure and corrosion behavior of 316L stainless steel fabricated by selective laser melting for proton exchange membrane fuel cells", *Electrochimica Acta*, Vol. 276, pp. 293-303.

Kurzynowski, T., *et al.* (2018), "Correlation between process parameters, microstructure and properties of 316 L stainless steel processed by selective laser melting", *Materials Science and Engineering: A*, Vol. 718, pp. 64-73.

Kusakin, P., *et al.* (2017), "On the effect of chemical composition on yield strength of TWIP steels", *Materials Science and Engineering: A*, Vol. 687, pp. 82-84.

La Fé-Perdomo, I., *et al.* (2023), "A novel optimization framework for minimizing the surface roughness while increasing the material processing rate in the SLM process of 316L stainless steel", *Rapid Prototyping Journal*, Vol. 29 No. 10.

Laleh, M., *et al.* (2021), "A critical review of corrosion characteristics of additively manufactured stainless steels", *International Materials Reviews*, Vol. 66 No. 8, pp. 563-599.

Laleh, M., *et al.* (2019), "On the unusual intergranular corrosion resistance of 316L stainless steel additively manufactured by selective laser melting", *Corrosion Science*, Vol. 161, p. 108189.

Leff, A.C. (2013), *Evaluation of Strain Effects of Grata Boundary Engineering Mechanisms Using In Situ TEM*, Drexel University, Philadelphia, PA.

Leicht, A., *et al.* (2020), "Effect of process parameters on the microstructure, tensile strength and productivity of 316L parts produced by laser powder bed fusion", *Materials Characterization*, Vol. 159, p. 110016.

Leicht, A., *et al.* (2020), "Effect of scan rotation on the microstructure development and mechanical properties of 316L parts produced by laser powder bed fusion", *Materials Characterization*, Vol. 163, p. 110309.

Liverani, E., *et al.* (2017), "Effect of selective laser melting (SLM) process parameters on microstructure and mechanical properties of 316L austenitic stainless steel", *Journal of Materials Processing Technology*, Vol. 249, pp. 255-263.

Lou, X., Andresen, P.L. and Rebak, R.B. (2018), "Oxide inclusions in laser additive manufactured stainless steel and their effects on impact toughness and stress corrosion cracking behavior", *Journal of Nuclear Materials*, Vol. 499, pp. 182-190.

Ma, C., *et al.* (2025), "A novel anti-corrosion strategy for ultra-high purity 316L stainless steel in the semiconductor industry: leveraging alternating voltage passivation and nitric acid passivation", *Corrosion Science*, Vol. 255, p. 113153.

Malik, A.W., Mahmood, M.A. and Liou, F. (2024), "Digital twin–driven optimization of laser powder bed fusion processes: a focus on lack-of-fusion defects", *Rapid Prototyping Journal*, Vol. 30 No. 10, pp. 1977-1988.

Marattukalam, J.J., *et al.* (2020), "The effect of laser scanning strategies on texture, mechanical properties, and site-specific grain orientation in selective laser melted 316L SS", *Materials & Design*, Vol. 193, p. 108852.

Mertens, A., *et al.* (2014), "Microstructures and mechanical properties of stainless steel AISI 316L processed by selective laser melting", *Materials Science Forum*, Vols 783-786.

Meyers, M.A. and Chawla, K.K. (2008), *Mechanical Behavior of Materials*, Cambridge university press, Cambridge, UK.

Moyle, M., *et al.* (2022), "Multi-scale characterisation of microstructure and texture of 316L stainless steel manufactured by laser powder bed fusion", *Materials Characterization*, Vol. 184, p. 111663.

Nabarro, F. (1997), "Fifty-year study of the Peierls-Nabarro stress", *Materials Science and Engineering: A*, Vols 234-236, pp. 67-76.

Ni, X., *et al.* (2018), "Corrosion behavior of 316L stainless steel fabricated by selective laser melting under different scanning speeds", *Journal of Materials Engineering and Performance*, Vol. 27 No. 7, pp. 3667-3677.

Niendorf, T., *et al.* (2013), "Highly anisotropic steel processed by selective laser melting", *Metallurgical and Materials Transactions B*, Vol. 44 No. 4, pp. 794-796.

Prashanth, K.G., *et al.* (2017), "Is the energy density a reliable parameter for materials synthesis by selective laser melting?", *Materials Research Letters*, Vol. 5 No. 6, pp. 386-390.

Read, N., *et al.* (2015), "Selective laser melting of AlSi10Mg alloy: process optimisation and mechanical properties development", *Materials & Design (1980-2015)*, Vol. 65, pp. 417-424.

Ronneberg, T., Davies, C.M. and Hooper, P.A. (2020), "Revealing relationships between porosity, microstructure and mechanical properties of laser powder bed fusion 316L stainless steel through heat treatment", *Materials & Design*, Vol. 189, p. 108481.

Röttger, A., *et al.* (2016), "Comparison of microstructure and mechanical properties of 316 L austenitic steel processed by selective laser melting with hot-isostatic pressed and cast material", *Materials Science and Engineering: A*, Vol. 678, pp. 365-376.

Salman, O., *et al.* (2019), "Effect of heat treatment on microstructure and mechanical properties of 316L steel synthesized by selective laser melting", *Materials Science and Engineering: A*, Vol. 748, pp. 205-212.

Sander, G., *et al.* (2017), "On the corrosion and metastable pitting characteristics of 316L stainless steel produced by selective laser melting", *Journal of The Electrochemical Society*, Vol. 164 No. 6, p. C250.

Schneck, M., *et al.* (2021), "Review on additive hybrid-and multi-material-manufacturing of metals by powder bed fusion: state of technology and development potential", *Progress in Additive Manufacturing*, Vol. 6 No. 4, pp. 1-14.

Sn, A.B. (2024), "A review on microstructure and mechanical properties of Inconel 625 alloy fabricated using wire arc additive manufacturing process", *Rapid Prototyping Journal*, Vol. 30 No. 7, pp. 1337-1347.

Sun, Z. (2019), "Additive manufacturing of austenitic alloys with high strength and high ductility by selective laser melting".

Sun, Z., *et al.* (2018), "Simultaneously enhanced strength and ductility for 3D-printed stainless steel 316L by selective laser melting", *NPG Asia Materials*, Vol. 10 No. 4, pp. 127-136.

Suryawanshi, J., Prashanth, K. and Ramamurty, U. (2017), "Mechanical behavior of selective laser melted 316L stainless steel", *Materials Science and Engineering: A*, Vol. 696, pp. 113-121.

Tapia, G. and Elwany, A. (2014), "A review on process monitoring and control in metal-based additive manufacturing", *Journal of Manufacturing Science and Engineering*, Vol. 136 No. 6, p. 60801.

Tasan, C.C., *et al.* (2015), "An overview of dual-phase steels: advances in microstructure-oriented processing and micromechanically guided design", *Annual Review of Materials Research*, Vol. 45 No. 1, pp. 391-431.

Tascioglu, E., Karabulut, Y. and Kaynak, Y. (2020), "Influence of heat treatment temperature on the microstructural, mechanical, and wear behavior of 316L stainless steel fabricated by laser powder bed additive manufacturing", *The International Journal of Advanced Manufacturing Technology*, Vol. 107 Nos 5-6, pp. 1947-1956.

Thijs, L., *et al.* (2013), "Fine-structured aluminium products with controllable texture by selective laser melting of pre-alloyed AlSi10Mg powder", *Acta Materialia*, Vol. 61 No. 5, pp. 1809-1819.

Van Bohemen, S. (2018), "Exploring the correlation between the austenite yield strength and the bainite lath thickness", *Materials Science and Engineering: A*, Vol. 731, pp. 119-123.

Wang, D., *et al.* (2016), "Investigation of crystal growth mechanism during selective laser melting and mechanical property characterization of 316L stainless steel parts", *Materials & Design*, Vol. 100, pp. 291-299.

Wang, Y.M., *et al.* (2018), "Additively manufactured hierarchical stainless steels with high strength and ductility", *Nature Materials*, Vol. 17 No. 1, pp. 63-71.

Wei, H., Mazumder, J. and DebRoy, T. (2015), "Evolution of solidification texture during additive manufacturing", *Scientific Reports*, Vol. 5 No. 1, p. 16446.

Wei, X., *et al.* (2022), "Enhanced corrosion resistance by engineering crystallography on metals", *Nature Communications*, Vol. 13 No. 1, p. 726.

Yadollahi, A., *et al.* (2015), "Effects of process time interval and heat treatment on the mechanical and microstructural properties of direct laser deposited 316L stainless steel", *Materials Science and Engineering: A*, Vol. 644, pp. 171-183.

Yan, H., *et al.* (2014), "Influence of shear banding on the formation of brass-type textures in polycrystalline FCC metals with low stacking fault energy", *Journal of Materials Science & Technology*, Vol. 30 No. 4, pp. 408-416.

Yin, Y., *et al.* (2019), "Mechanism of high yield strength and yield ratio of 316 L stainless steel by additive manufacturing", *Materials Science and Engineering: A*, Vol. 744, pp. 773-777.

Zeng, Q., Gan, K. and Wang, Y. (2021), "Effect of heat treatment on microstructures and mechanical behaviors of 316L stainless steels synthesized by selective laser melting", *Journal of Materials Engineering and Performance*, Vol. 30 No. 1, pp. 409-422.

Zhang, X., *et al.* (2020), "Simulation and experimental studies on process parameters, microstructure and mechanical properties of selective laser melting of stainless steel 316L", *Journal of the Brazilian Society of Mechanical Sciences and Engineering*, Vol. 42 No. 8, pp. 1-14.

Zhou, C., *et al.* (2020), "Improvement of corrosion resistance of SS316L manufactured by selective laser melting through subcritical annealing", *Corrosion Science*, Vol. 164, p. 108353.

Supplementary material

The supplementary material for this article can be found online.

Corresponding author

Mahyar Khorasani can be contacted at: mahyar.khorasani@rmit.edu.au